ELSEVIER

Materials Science and Engineering A 413–414 (2005) 485–489

MATERIALS SCIENCE & ENGINEERING A

www.elsevier.com/locate/msea

A way of coupling ternary phase diagram information with multiphase solidification simulations

A. Ludwig, M. Gruber-Pretzler*, F. Mayer, A. Ishmurzin, M. Wu

Christian-Doppler Laboratory for Multiphase Modeling of Metallurgical Processes, Department of Metallurgy, University of Leoben, Franz-Josef-Str. 18, A-8700 Leoben, Austria

Received in revised form 20 July 2005

Abstract

Multiphase solidification simulations have become a powerful tool of modeling various aspects of metallic solidification like thermo-solutal convection, feeding flow, macrosegregations and others. However, a necessary step towards practical application is the consideration of multi-componental phase diagram information. In the present paper, a general concept is presented which shows how the primary solidification can be modeled by using ternary and higher componental phase diagram information in combination with multiphase process simulation. Based on the presented approach, first results on the formation of macrosegregations during continuous casting of technical bronze alloys are presented.

Keywords: Phase diagram; Simulations; Solidification

1. Introduction

For almost all practical solidification processes, inhomogeneous distributions of alloy elements at the scale of the whole casting, known as macrosegregations, are found. In order to predict the formation of those undesired 'defects', numerical methods have been developed intensively during the last years [1–12]. In a recent publication [13], the columnar-to-equiaxed transition has been modeled with a three-phase volume averaging approach, where the motion of grains, the melt-flow caused by shrinkage and thermo-solutal buoyancy and the growth of a columnar front perpendicular to the isotherms were considered. However, the predicted macrosegregations was for binary alloys only.

On the other hand, since the pioneer work of Kaufman and Bernstein [14], the calculation of phase diagrams has become a widely used tool for predicting thermodynamic information by computational techniques. This method is known as the CALPHAD method (calculation of phase diagrams). Nowadays, more and more groups have started to combine numerical solidification simulations with CALPHAD calculations [15–18].

In the present paper, a way of coupling ternary and higher componental phase diagram information with the multiphase solidification approach proposed in Ref. [13] is presented. As we will concentrate in details on the coupling, the used multiphase solidification approach is not outlined here. The reader is referred to the original publication for details. However, it is important to mention, that for the examples shown here, we have used only the columnar solidification part of the three-phase approach, where the permeable mushy zone is thought to be composed of cylindrical 'dendrites' with a given dendrite arm spacing, λ_1. We have taken into account feeding flow through the mushy zone, but we have neglected thermo-solutal flow.

2. Model description

The three-phase volume averaging model proposed by the authors in Ref. [13] considers three interpenetration continua: the melt, $i = l$ (liquid), globular equiaxed grains, $i = e$ and columnar dendrite trunks, $i = c$. For each of these three phases, the conservation equations for mass, momentum, enthalpy and $j = 1, \ldots, n$ different species are solved, to estimate the volume fraction f_i, the phase velocity $\vec{u}_i$, the phase enthalpy h_i, and the average mass fraction of the j-species c_i^j in phase i. From the different enthalpies, a single temperature, T, is calculated.

The proposed solidification model considers the growth of spherical equiaxed grains and cylindrical columnar dendrites.

* Corresponding author. Tel.: +43 38424025223.
E-mail address: monika.gruber-pretzler@notes.uniledren.ac.at (M. Gruber-Pretzler).

0921-5093/$ – see front matter © 2005 Published by Elsevier B.V.
doi:10.1016/j.msea.2005.09.012

At the interface, the grains/dendrites have a species mass fraction of $\tilde{c}_l^j$ in the liquid and $\tilde{c}_s^j = \tilde{c}_e^j$ in the spherical solid and in the cylindrical solid. The assumption of a quasi-steady state diffusion field around growing spheres/cylinders of diameter d leads to the following expression for the solute gradient, $\tilde{G}_l^j$, of the j-species in the liquid at the interface

$$\tilde{G}_l^j = \begin{cases} -\dfrac{\tilde{c}_l^j - c_l^j}{d/2}, & \text{for spherical growth} \\ -\dfrac{\tilde{c}_l^j - c_l^j}{d/2} \ln^{-1}\left(\dfrac{\lambda_1}{d}\right), & \text{for cylindrical growth} \end{cases} \quad (1)$$

Neglecting the solute diffusion from the interface into the solid, the solute flux balance at the interface leads to an expression for the growth velocity v

$$v(\tilde{c}_l^j - \tilde{c}_s^j) = -D_j \tilde{G}_l^j \Rightarrow v = \begin{cases} \dfrac{2D_j}{d}\dfrac{\tilde{c}_l^j - c_l^j}{\tilde{c}_l^j - \tilde{c}_s^j}, & \text{for spherical growth} \\ \dfrac{2D_j}{d}\dfrac{\tilde{c}_l^j - c_l^j}{\tilde{c}_l^j - \tilde{c}_s^j} \ln^{-1}\left(\dfrac{\lambda_1}{d}\right), & \text{for cylindrical growth} \end{cases} \quad (2)$$

with D_j being the diffusion coefficient of the j-species in the liquid. In case of strong convection, Eq. (2) has to be modified by including the Sherwood-Number. Note that Eq. (2) is valid for all considered species $j = 1, \ldots, n$. However, to estimate v, only one equation is needed. The additional $n-1$ equations can be combined to give

$$v = v_1(\tilde{c}_l^1, c_l^1, \tilde{c}_s^1) = v_j(\tilde{c}_l^j, c_l^j, \tilde{c}_s^j), \quad \text{with } j = 2, \ldots, n, \quad (3)$$

where a generalized form is used. Knowing the growth velocity v, the mass transfer, M_{ls}, can be expressed as

$$M_{ls} = \begin{cases} \rho_s v (n\pi d^2)(1 - f_s), & \text{for spherical growth} \\ \rho_s v \left(\dfrac{\pi d}{\lambda_1^2}\right)(1 - f_s), & \text{for cylindrical growth} \end{cases} \quad (4)$$

where ρ_s indicates the density of the solid and the Avrami-factor $(1 - f_s)$ accounts for the impingement of the grains/dendrites while the solidification proceeds, n the number density of spherical grains gained from the solution of a corresponding conservation equation and λ_1 represents the dendrite arm spacing. A mass transfer, M_{ls}, during solidification is always accompanied with a species transfer, C_{ls}^j (solute rejection), of the form

$$C_{ls}^j = c^{*j} M_{ls}, \quad \text{with } c^{*j} = \begin{cases} \tilde{c}_s^j & \text{for solidification} \\ c_s^j & \text{for melting} \end{cases} \quad (5)$$

To estimate v via Eq. (2), the interface species mass fraction, $\tilde{c}_l^j$ and $\tilde{c}_s^j$ with $j = 1, \ldots, n$, have to be determined by thermodynamic considerations. As the temperature around the growing grains/dendrites is known from the solution of the enthalpy conservation equations, the thermodynamic equilibrium condition, g_j (tie lines), yields the following relations

$$\tilde{c}_s^j = g_j(\tilde{c}_l^1, \ldots, \tilde{c}_l^n, T), \quad \text{with } j = 1, \ldots, n \quad (6)$$

which can be used to estimate the n-species mass fraction at the solid side of the interface, $\tilde{c}_s^j$, from the liquid side counterparts. In addition, it has to be stated that for the single-phase solidification process considered here, the $\tilde{c}_l^j$'s are not independent of each other. So, the thermodynamic gives a relation, h, which might look as

$$\tilde{c}_l^1 = h(\tilde{c}_l^2, \ldots, \tilde{c}_l^n, T) \quad (7)$$

The $n-1$ equations, Eq. (3), the n equations, Eqs. (6) and (7) yield a non-linear system of equations, which can be used to estimate the $2n$ interface quantities $\tilde{c}_l^1, \ldots, \tilde{c}_l^n, \tilde{c}_s^1, \ldots, \tilde{c}_s^n$ (thermodynamic) from the $n+1$ bulk quantities $c_l^1, \ldots, c_l^n, T$ (process). Note that the $n+1$ bulk quantities are determined from solving the corresponding conservation equations.

The above non-linear system of equations is the key point in the present paper. It can be solved exactly in cases were the process simulations (from which $c_l^1, \ldots, c_l^n, T$ is gained) is online coupled with a thermodynamic program (from which the functions g_j and h are known). However, a way to solve this non-linear system of equations much faster but only approximately is to solve the corresponding linearized form around the first point were solid nucleate and grow. That is at the liquidus temperature of the initial alloy, $T_L(c_0^1, \ldots, c_0^n)$, and at its initial composition, $c_0^1, \ldots, c_0^n$.

2.1. Linearization

Linearization of Eq. (3), (6) and (7) around T_L for $n = 2$ alloying elements gives:

$$\Delta v = \tilde{\gamma}_l^\alpha \Delta\tilde{c}_l^\alpha + \gamma_l^\alpha \Delta c_l^\alpha + \tilde{\gamma}_s^\alpha \Delta\tilde{c}_s^\alpha = \tilde{\gamma}_l^\beta \Delta\tilde{c}_l^\beta + \gamma_l^\beta \Delta c_l^\beta + \tilde{\gamma}_s^\beta \Delta\tilde{c}_s^\beta \quad (8)$$

$$\Delta\tilde{c}_s^\alpha = k_\alpha \Delta\tilde{c}_l^\alpha + k_\alpha m_{l,\alpha}^{-1} m_{l,\beta} \Delta\tilde{c}_l^\beta + k_\alpha m_{l,\alpha}^{-1} \Delta T \quad (9)$$

$$\Delta\tilde{c}_s^\beta = k_\beta m_{l,\beta}^{-1} m_{l,\alpha} \Delta\tilde{c}_l^\alpha + k_\beta \Delta\tilde{c}_l^\beta + k_\beta m_{l,\beta}^{-1} \Delta T \quad (10)$$

$$m_{l,\alpha} \Delta\tilde{c}_l^\alpha = m_{l,\beta} \Delta\tilde{c}_l^\beta + \Delta T \quad (11)$$

with the abbreviations

$$k_\alpha = \frac{\partial\tilde{c}_s^\alpha}{\partial\tilde{c}_l^\alpha}, \qquad k_\beta = \frac{\partial\tilde{c}_s^\beta}{\partial\tilde{c}_l^\beta}, \quad (12)$$

$$m_{l,\alpha}^{-1} = \frac{\partial\tilde{c}_l^\alpha}{\partial T}, \qquad m_{l,\beta}^{-1} = \frac{\partial\tilde{c}_l^\beta}{\partial T}, \quad (13)$$

which accounts for the thermodynamic at the interface. The transformation kinetic expressed as diffusion-limited flux away from the solid–liquid interface is account for in the terms

$$\gamma_l^j = \frac{\partial v_j}{\partial c_l^j} = -\frac{2D_j}{d}\frac{1}{\tilde{c}_l^j - \tilde{c}_s^j} \quad (14)$$

$$\tilde{\gamma}_l^j = \frac{\partial v_j}{\partial \tilde{c}_l^j} = \frac{2D_j}{d}\left(\frac{1}{\tilde{c}_l^j - \tilde{c}_s^j} - \frac{\tilde{c}_l^j - c_l^j}{(\tilde{c}_l^j - \tilde{c}_s^j)^2}\right) \quad (15)$$

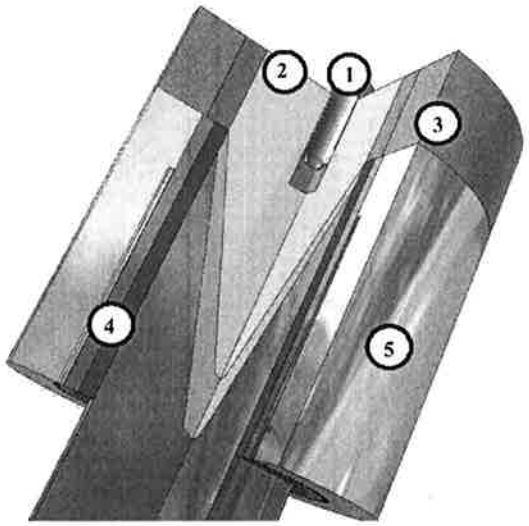

Fig. 1. Continuous casting: ① nozzle; ② free surface; ③ graphite mold with isolation; ④ graphite and copper mold; ⑤ steel mold with water cooling.

$$\tilde{\gamma}_s^j = \frac{\partial v_j}{\partial \tilde{c}_s^j} = \frac{2D_j}{d}\frac{\tilde{c}_l^j - c_l^j}{(\tilde{c}_l^j - \tilde{c}_s^j)^2} \tag{16}$$

Eqs. (14)–(16) are for spherical growth, the corresponding terms for cylindrical growth are straight forward. Eqs. (8)–(11) can be written as system of equations for the four unknown quantities $\Delta\tilde{c}_l^\alpha$, $\Delta\tilde{c}_l^\beta$, $\Delta\tilde{c}_s^\alpha$ and $\Delta\tilde{c}_s^\beta$

$$\begin{pmatrix} \tilde{\gamma}_l^\alpha & -\tilde{\gamma}_l^\beta & \tilde{\gamma}_s^\alpha & -\tilde{\gamma}_s^\beta \\ k_\alpha & k_\alpha m_{l,\alpha}^{-1} m_{l,\beta} & -1 & 0 \\ k_\beta m_{l,\beta}^{-1} m_{l,\alpha} & k_\beta & 0 & -1 \\ m_{l,\alpha} & -m_{l,\beta} & 0 & 0 \end{pmatrix} \begin{pmatrix} \Delta\tilde{c}_l^\alpha \\ \Delta\tilde{c}_l^\beta \\ \Delta\tilde{c}_s^\alpha \\ \Delta\tilde{c}_s^\beta \end{pmatrix}$$
$$= \begin{pmatrix} -\gamma_{l\alpha} & \gamma_{l\beta} & 0 \\ 0 & 0 & -k_\alpha m_{l,\alpha}^{-1} \\ 0 & 0 & -k_\beta m_{l,\beta}^{-1} \\ 0 & 0 & 1 \end{pmatrix} \begin{pmatrix} \Delta c_l^\alpha \\ \Delta c_l^\beta \\ \Delta T \end{pmatrix} \tag{17}$$

As at the starting of solidification, the far field concentration is equal to the interface concentration, $c_l^j = \tilde{c}_l^j$, the derivation Eqs. (15) and (16) for spherical growth at T_L, c_0^α, c_0^β are simply

$$\tilde{\gamma}_{lj} = \frac{2D_j}{d}\frac{1}{c_0^j - c_{s,0}^j}, \quad \tilde{\gamma}_{sj} = 0. \tag{18}$$

2.2. Considered process parameters

For the process simulation of continuous casting of a technical bronze alloy, a casting velocity of $V_{cast} = 1.9$ mm/s and casting temperature of $T_0 = 1389$ K is considered. Due to the cylindrical shape of the mold, an axis symmetric simulation has been chosen. The mold is schematically shown in Fig. 1 where (①) gives the position of the nozzle, (②) indicates the free surface on the top, (③) shows the upper part of the graphite mold which is insulating, (④) shows the lower part of the graphite mold which is surrounded (⑤) by a copper–steel mold including a water cooling. In Fig. 2, the boundary conditions are shown. (①) gives the position of the inlet, where a constant pressure is applied as boundary condition (pressure inlet). A heat transfer coefficient (HTC) of $h = 50$ W/(m^2 K) and a nozzle temperature of $T_{SEN} = 1292$ K is taken for the submerged entry nozzle (SEN) region. For (②), HTC and temperature have a value of $h = 50$ W/(m^2 K) and $T_{surface} = 325$ K. For (③), almost ideal insulation is assumed with $h = 10$ W/(m^2 K) and $T_{mold} = 1292$ K. (④) has $h = 3000$ W/(m^2 K) and $T_{mold} = 550$ K and (⑤) has $h = 1000$ W/(m^2 K) and $T_{water} = 300$ K. For the outlet (⑥), the casting velocity V_{cast} is taken as boundary condition (velocity outlet). For the nozzle, a non-slip condition and for the free surface, a slip condition is used. The wall of the mold is assumed to move with the casting velocity. Here, a slip condition for the liquid phase and a non-slip condition for the columnar phase have been chosen. A grid of 9016 cells and 9296 nodes is used.

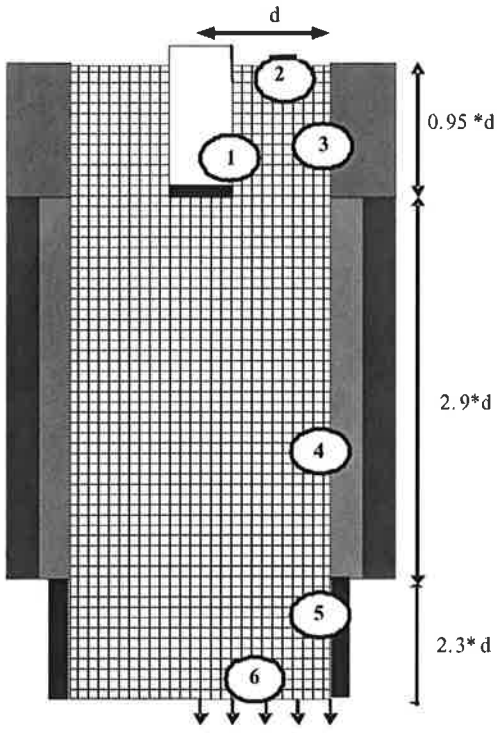

Fig. 2. Grid and interfaces for boundary conditions (details given in the text).

As initial conditions, we start with hot melt ($T_{init} = 1389$ K) in rest ($V_{init} = 0$ m/s). Cooling and inflow are then resulting in the formation of a solidifying shell and an acceleration of the melt in the core of the strand, until steady state. The results presented in the next section are those for steady state.

3. Results and discussion

Fig. 3 shows the temperature (a), the volume fraction of solid (b), the strength of the velocity of the melt (c), the average solid Sn-concentration (d) and the average melt Sn-concentration (e), $t = 633$ s after switching on cooling and inflow. The temperature field reflects the applied boundary conditions. The isolines plotted are liquidus ($T_L = 1289$ K), solidus ($T_S = 1230$ K) and the

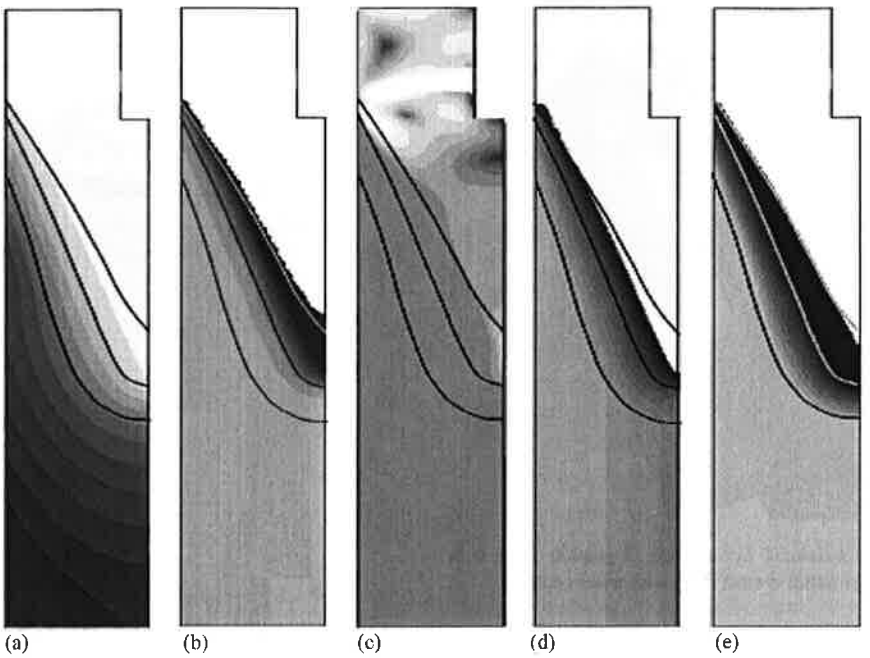

Fig. 3. Predicted steady state distribution of: (a) temperature (black: 600 K; white: 1389 K); (b) volume fraction of columnar phase (black: 10^{-6}%; bright gray: 100%); (c) strength of melt velocity (white: 0.025 m/s; black: 9.25×10^{-6} m/s); (d) average concentration of the columnar phase (black: 3.5%; gray: 5.27%); (e) average melt concentration (black: 6%; gray: 25.5%). The liquidus and solidus temperature together with the temperature at which the considered alloy is completely solidified are also shown with isolines.

final temperature for solidification of the technical bronze considered ($T_P = 1072$ K).

Within the columnar mushy zone, located between T_L and T_P, the volume fraction of solid varies from 0 to 1. As we considered the mush to be permeable, melt-flow occurs through the mush. However, the flow velocities in the mush are much smaller compared to the inlet flow. The incoming melt reveals a velocity as high as $V_{in} = 25$ mm/s. This large value is a consequence of the constant outlet velocity, V_{cast}, and the overall mass conservation. The inlet jets hit the mold close to the region where first solid forms, bend inwards and form so corresponding vortices. Beside the inlet jets with the corresponding vortices, another high velocity region appears at the symmetry plane deep down in the pool (see Fig. 4). Here, the solidification shrinkage leads to strong flow because the cross section for feeding is relatively small compared to the large solidifying area near the center of the cylindrical casting.

Feeding flow caused by solidification shrinkage leads to a solute transport from the dendrite tip region into the mush towards the roots of the dendrites. Since the early work of Fem-

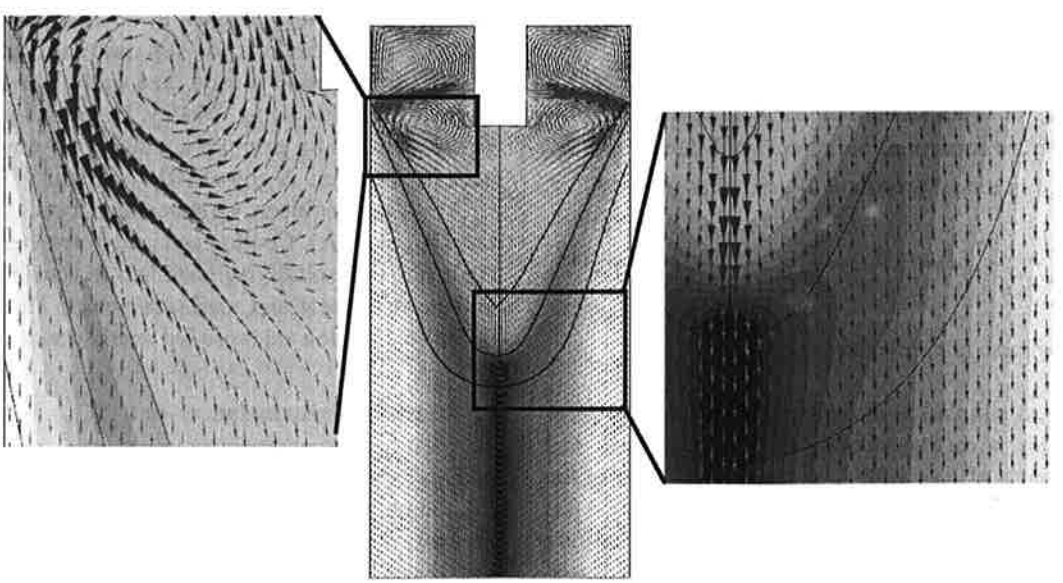

Fig. 4. Predicted macrosegregations expressed in terms of mixture concentration (Eq. (19)) (white; bright gray: positive macrosegregation, black: negative macrosegregation). The liquidus and solidus temperature together with the temperature at which the considered alloy is completely solidified are also shown with isolines.

ings [19,20], this phenomenon is known to result in a positive macrosegregation, the so-called inverse segregation, at the surface of a casting. In Fig. 4, the predicted Sn macrosegregations are shown in terms of

$$c_{\mathrm{mix}} = \frac{c_{\mathrm{l}} f_{\mathrm{l}} \rho_{\mathrm{l}} + c_{\mathrm{s}} f_{\mathrm{s}} \rho_{\mathrm{s}}}{f_{\mathrm{l}} \rho_{\mathrm{l}} + f_{\mathrm{s}} \rho_{\mathrm{s}}} \tag{19}$$

together, the T_{L}, T_{S} and T_{P} isolines and the flow velocity of the melt. The mush which forms near the mold wall is fed with 'its own' segregated melt, which is in fact the idea behind Femings' explanation. On the other hand, for the center region, the amount of 'own' melt is fare away from being enough to feed the large solidifying area at the center. Therefore, the center region is fed with more or less non-segregated 'fresh' melt from the melt pool and so a strong negative segregated area occurs in the center.

4. Conclusions

The paper presents a method of coupling thermodynamic calculations with multiphase process simulations. Besides the direct coupling, an approximate way is suggested where a bunch of parameters (accounting for thermodynamics and diffusion-kinetics) are sufficient to consider for the multi-componental nature of technical alloys in the process simulation. In the presented example of continuous casting of a bronze alloy, it was demonstrated how process dynamic may influence average liquid and solid concentration and with that lead to the formation of macrosegregations.

Acknowledgement

This work was financially supported by the Austria Christian-Doppler Society (CDG) for which the authors kindly acknowledge.

Appendix A

List of symbols

c_i^j mass fraction of the j-species in phase i
$\tilde{c}_i^j$ mass fraction of the j-species at the interface melt/phase i
C_{ls}^j species transfer of species j between liquid/solid
c_{mix} mixture concentration (macrosegregation)
$\Delta\tilde{c}_{\mathrm{l}}^{\alpha}$, $\Delta\tilde{c}_{\mathrm{l}}^{\beta}$, $\Delta\tilde{c}_{\mathrm{s}}^{\alpha}$, $\Delta\tilde{c}_{\mathrm{s}}^{\beta}$ changes in the concentration in liquid and solid adjacent to the solid/liquid interface for the species α and β
d diameter of the spherical/cylindrical solid
D_j diffusion coefficient of the j-species in the liquid
f_i volume fraction of phase i
$\tilde{G}_{\mathrm{l}}^j$ solute gradient at the liquid side of the solid/liquid interface for species j
g_i, h thermodynamic functions
h heat transfer coefficient (HTC)
h_i phase enthalpy of phase i
k_α, k_β generalized redistribution coefficient for the species α and β
$m_{\mathrm{l},\alpha}$, $m_{\mathrm{l},\beta}$ liquidus slope for the species α and β
M_{ls} mass transfer rate liquid/solid
n number density of spherical/cylindrical solid
ρ_{s} density of the solid
T temperature
T_{L} liquidus temperature
T_{init} initial temperature
T_{mold} mold temperature
T_{P} final temperature for solidification
T_{S} solidus temperature
T_{SEN} nozzle temperature
T_{surface} surface temperature
T_{water} water temperature
$\vec{u}_i$ phase velocity of phase i
v growth velocity
V_{cast} casting velocity
V_{in} inlet velocity
V_{init} initial velocity
λ_1 dendrite arm spacing
$\gamma_{\mathrm{l}j}$, $\tilde{\gamma}_{\mathrm{l}j}$, $\tilde{\gamma}_{\mathrm{s}j}$ kinetic transformation terms

References

[1] M. Rappaz, Int. Mater. Rev. 34 (1989) 93–123.
[2] J. Ni, C. Beckermann, Metall. Trans. 22B (1991) 349–361.
[3] C. Beckermann, R. Viskanta, Appl. Mech. Rev. 46 (1993) 1–27.
[4] J. Ni, F.P. Incropera, Int. J. Heat Mass Transfer 38 (1995) 1271–1284.
[5] J. Ni, F.P. Incropera, Int. J. Heat Mass Transfer 38 (1995) 1285–1296.
[6] C.Y. Wang, C. Beckermann, Metall. Mater. Trans. 27A (1996) 2754–2764.
[7] C.Y. Wang, C. Beckermann, Metall. Mater. Trans. 27A (1996) 2765–2783.
[8] C.Y. Wang, C. Beckermann, Metall. Mater. Trans. 27A (1996) 2784–2795.
[9] C. Beckermann, JOM 49 (1997) 13–17.
[10] A.V. Reddy, C. Beckermann, Metall. Mater. Trans. B 28 (1997) 479–489.
[11] A. Ludwig, M. Wu, Metall. Mater. Trans. A 33 (2002) 3673–3683.
[12] M. Wu, A. Ludwig, A. Bührig-Polaczek, M. Fehlbier, P.R. Sahm, Int. J. Heat Mass Transfer 46 (2003) 2819–2832.
[13] M. Wu, A. Ludwig, Metall. Mater. Trans., in press.
[14] L. Kaufman, H. Bernstein, Computer Calculation of Phase Diagrams with Special Reference to Refractory Metals, Academic Press, New York, 1970.
[15] U. Kattner, JOM 49 (12) (1997) 14–19.
[16] K. Greven, A. Ludwig, T. Hofmeister, P.R. Sahm, in: A. Ludwig (Ed.), Solidification of Metallic Melts in Research and Technology, Wiley-VCH, Weinheim, 1999, p. 119.
[17] U. Grafe, B. Böttger, J. Tiaden, S.G. Fries, Scr. Mater. 42 (2000) 1179–1186.
[18] W.J. Boettinger, S.R. Coriell, A.L. Greer, A. Karma, W. Kurz, M. Rappaz, R. Trivedi, Acta Mater. 48 (2000) 43–70.
[19] M.C. Femings, G.E. Nereo, Trans. Metall. Soc. AIME 239 (1967) 1449–1460.
[20] M.C. Femings, R. Mehrabian, G.E. Nereo, Trans. Metall. Soc. AIME 242 (1967) 41–49.